UOCS –VIII. UV study of the open cluster NGC 2506 using *ASTROSAT*[★]

Anju Panthi,[1][†] Kaushar Vaidya [ID],[1][†] Vikrant Jadhav [ID],[2,3,4][†] Khushboo K. Rao [ID],[1]
Annapurni Subramaniam,[2] Manan Agarwal [ID][5] and Sindhu Pandey [ID][6]

[1]*Department of Physics, Birla Institute of Technology and Science, Pilani 333031, India*
[2]*Indian Institute of Astrophysics, Sarjapur Road, Koramangala, Bangalore 560034, India*
[3]*Joint Astronomy Programme and Department of Physics, Indian Institute of Science, Bangalore 560012, India*
[4]*Inter-University Centre for Astronomy and Astrophysics, Post Bag 4, Ganeshkhind, Pune, Maharashtra 411007, India*
[5]*Department of Physics and Kavli Institute for Astrophysics and Space Research, Massachusetts Institute of Technology, Cambridge, MA 02139, USA*
[6]*Aryabhatta Research Institute of Observational Sciences, Manora Peak, Nainital 263001, India*

ABSTRACT

We study an intermediate-age open cluster (OC) NGC 2506 using the *ASTROSAT*/UVIT data and other archival data. We identified 2175 cluster members using a machine learning-based algorithm, ML–MOC, on *Gaia* EDR3 data. Among the cluster members detected in UVIT filters, *F148W*, *F154W*, and *F169M*, we detect nine blue straggler stars (BSS), three yellow straggler stars (YSS), and three red clump (RC) stars. We construct multiwavelength spectral energy distributions (SEDs) of these objects to characterize them and to estimate their parameters. We discovered hot companions to three BSS, two YSS, and three RC candidates and estimated their properties. The hot companions with estimated temperatures, $T_{eff} \sim 13250$–$31\,000$ K, are WDs of extremely low mass (ELM, ~ 0.20 M$_\odot$), low mass (LM, ~ 0.20–0.40 M$_\odot$), normal mass (~ 0.40–0.60 M$_\odot$), and high mass (~ 0.8 M$_\odot$). We suggest that systems with ELM and LM WDs as companions are formed via Case-A/Case-B mass transfer mechanism. A BSS is the likely progenitor of the high-mass WD, as a star with more than the turn-off mass of the cluster is needed to form a high-mass WD. Thus, systems with a high-mass WD are likely to be formed through merger in triple systems. We conclude that mass transfer as well as merger pathways of BSS formation are present in this cluster.

Key words: binaries: general – blue stragglers – white dwarfs – open clusters and associations: individual: NGC 2506 – ultraviolet: stars.

1 INTRODUCTION

Star clusters are ideal laboratories to study stellar populations in the host galaxy. Being a homogenous collection of stars having the same age, distances, kinematics, and metallicities, they provide the means to study the single and binary evolution of stars. Blue straggler stars (BSS) are unusual stellar populations that are brighter and bluer with respect to the main-sequence turn-off (MSTO) in the colour–magnitude diagrams (CMD) of star clusters (Sandage 1953). They are found in different stellar environments such as open clusters (OCs; Ahumada & Lapasset 1995), globular clusters (GCs; Sandage 1953), Galactic fields (Preston & Sneden 2000), and dwarf galaxies (Momany et al. 2007). BSS in star clusters are linked to the presence of close binary or multiple stellar systems, which are often formed through internal binary evolution or during the dynamical interaction between binaries and other stars (Knigge, Leigh & Sills 2009; Mathieu & Geller 2009; Leigh, Sills & Knigge 2011). Observational evidence shows that BSS are among the most massive members of star clusters (Shara, Saffer & Livio 1997; Gilliland et al. 1998; Beccari et al. 2006; Ferraro et al. 2006; Fiorentino et al. 2014) and therefore they tend to get concentrated toward the cluster centre as

the cluster evolves (Ferraro, Fusi Pecci & Buonanno 1992; Ferraro et al. 2012; Vaidya et al. 2020; Rao et al. 2021). Due to this, BSS are considered crucial probes to study the interplay between stellar evolution and stellar dynamics (Bailyn 1995).

The three processes, namely direct stellar collision (Chatterjee et al. 2013), mass transfer in a binary system (McCrea 1964), and merging in hierarchical triple stars (Perets & Fabrycky 2009), are anticipated to be the primary ways in which BSS are produced. Stellar collisions are likely to occur in the environments where stellar density is quite high, such as the cores of GCs (Hurley et al. 2005; Chatterjee et al. 2013; Hypki & Giersz 2013). The mass transfer mechanism may be further classified into three categories depending upon the evolutionary stage of the primary star when the mass transfer happens: Case-A, in which the primary is in the main sequence (MS; Webbink 1976), Case-B, in which the primary is in the red giant branch (RGB) phase (McCrea 1964), and Case-C, in which the primary is in the asymptotic giant branch (AGB) phase (Chen & Han 2008). The Case-A mass-transfer channel leaves behind either a single BSS or a binary BSS with a short-period, MS companion, Case-B mass-transfer channel produces a short-period (< 100 d) binary BSS with He WD as a companion, whereas Case-C mass transfer channel results in a long-period binary (> 1000 d) BSS with CO WD as a companion. In the case of merger in a hierarchical triple system, the dynamical evolution of the triples through the Kozai mechanism and tidal friction can induce the formation of very close

Table 1. Parameters of NGC 2506 from the literature.

Age (Gyr)	Distance (pc)	$E(B-V)$	[Fe/H]
1.1–3.4	3110–3880	0.04–0.08	− 0.52 to −0.19

Notes. Age: McClure, Twarog & Forrester (1981), Xin & Deng (2005), Anthony-Twarog, Deliyannis & Twarog (2016), Vaidya et al. (2020), Knudstrup et al. (2020) Distance: Kharchenko et al. (2013), Rangwal et al. (2019), Vaidya et al. (2020), Knudstrup et al. (2020) E(B-V): McClure et al. (1981), Kim et al. (2001), Carretta et al. (2004), Xin & Deng (2005), Anthony-Twarog et al. (2016), Knudstrup et al. (2020) [Fe/H]: Friel & Janes (1993), Reddy, Giridhar & Lambert (2012), Anthony-Twarog et al. (2018), Knudstrup et al. (2020).

inner binaries. Angular momentum loss in a magnetized wind or stellar evolution could then lead to the merger of these binaries (or to mass transfer between them) and produce BSS in long binary (or triple) systems (Kiseleva, Eggleton & Mikkola 1998; Fabrycky & Tremaine 2007).

Identification and characterization of BSS in OCs and GCs to infer their formation mechanism continues to be an important topic of research. Ultraviolet (UV) wavelengths are particularly suitable to study BSS, as BSS are much brighter in UV wavelengths owing to their relatively higher temperatures. Thus, in the UV wavelengths, the BSS define a clean sequence that is easily distinguishable in the CMD (Siegel et al. 2014; Ferraro et al. 2018). A study illustrating the above by Sahu et al. (2018) found that BSS sequence stands out in the UV CMDs as compared to the optical CMDs. Additionally, UV-based studies allow the possibility of identifying BSS binaries with a hot companion from the excess flux in the UV wavelengths. Knigge et al. (2000) identified a BSS-white dwarf (WD) binary in 47 Tuc obtained with the *Hubble Space Telescope (HST)* observations. In the OC NGC 188, Gosnell et al. (2015) discovered WD companions of seven BSS using *HST* observations in far-ultraviolet (FUV) filters. For the same cluster, Subramaniam et al. (2016a) discovered a post-AGB/HB companion of a BSS (WOCS 5885) using *ASTROSAT*/Ultraviolet Imaging Telescope (UVIT) data. Similarly, Sindhu et al. (2019), Pandey, Subramaniam & Jadhav (2021), Jadhav et al. (2021b), and Vaidya et al. (2022) used UVIT data to study the OCs M67, King 2, and NGC 7789, respectively, and reported BSS with hot companions. UV observations also detect other interesting objects in star clusters, such as the yellow straggler stars (YSS) and red clump (RC) stars. YSS are found blueward of the RGB and above the subgiant branch in the optical CMDs (Stryker 1993; Clark, Sandquist & Bolte 2004). These are significantly brighter than the MS, but redder than the blue stragglers (Landsman et al. 1997; Leiner et al. 2016), and are potentially the blue stragglers that have evolved into the giant or subgiant stars. Recently, YSS were found in an OC M67 using the *ASTROSAT*/UVIT data (Sindhu et al. 2019). The RC stars are cool horizontal branch stars that have undergone a helium flash and are now fusing helium in their cores. They appear red and close to the RGB (Girardi 2016).

NGC 2506 ($\alpha = 8^{\rm h}00^{\rm m}1^{\rm s}0, \delta = -10°46'12''$) is an intermediate-age (~ 2 Gyr) OC. Several photometric and spectroscopic studies have been done to estimate cluster parameters including age, distance, reddening, and metallicity that are listed in Table 1. Moreover, the BSS of this cluster have been identified in several studies (Xin & Deng 2005; Arentoft et al. 2007; Knudstrup et al. 2020; Vaidya et al. 2020; Jadhav & Subramaniam 2021; Rain, Ahumada & Carraro 2021), but they have not been studied so far using the UV-wavelengths. The

formation mechanisms of these BSS have also not been investigated earlier. We present the first UV-led multiwavelength study of the BSS populations in NGC 2506 using the *ASTROSAT*/ UVIT data. In addition to the BSS, we characterize the YSS and the RC stars of the cluster using multiwavelength data.

This paper is arranged in the following manner: Section 2 describes the observations and data reduction procedure, Section 3 gives the data analysis, Section 4 gives results and discussions, and Section 5 gives the conclusions of the work.

2 OBSERVATIONS AND DATA REDUCTION

UVIT is one of the payloads in *ASTROSAT* and has two 38-cm telescopes. One of the telescopes carries a far-UV (FUV) channel (130–180 nm), and the other carries both a near-UV (NUV) channel (200–300 nm) and a visible (VIS) channel (350–550 nm). UVIT can perform simultaneous observations in these three channels in a circular field of view of diameter ∼ 28 arcmin. It has a spatial resolution (FWHM) of ∼1.2 arcsec for the NUV filter and ∼1.5 arcsec for the FUV filter. The peak effective area excluding the losses in the filters used for band-selection of UVIT is ∼ 10 cm^2 for the FUV and ∼ 50 cm^2 for the NUV filter. The details of the UVIT instrument and calibration can be found in Kumar et al. (2012), Subramaniam et al. (2016b), and Tandon et al. (2017). NGC 2506 was observed on 2019 October 7, under the *ASTROSAT* proposal A07-005.

We obtained the science ready images from level 1 data available in the *ASTROSAT* archive by doing distortion correction, flat-field correction, and spacecraft drift using CCDLAB (Postma & Leahy 2017, 2021). The final science ready images in three FUV filters *F148W*, *F154W*, and *F169M* have exposure times of 9224, 7499, and 7027 s, respectively. These images were good for further analysis with an FWHM of ∼1 arcsec as mentioned in Table 2. We performed the point spread function (PSF) photometry on all the three UVIT images using the DAOPHOT package in IRAF (Stetson 1987). The UVIT magnitudes were obtained in the AB magnitude system by using the zero-point (ZP) magnitudes given in Tandon et al. (2020). The aperture correction value in each filter was estimated using the curve of growth analysis technique and was applied to the PSF magnitudes. We also applied the saturation corrections to the magnitudes following Tandon et al. (2020). The magnitudes and errors of detected sources are shown in Fig. 1.

3 DATA ANALYSIS

3.1 Cluster membership

In order to identify the members of NGC 2506, we used the machine learning-based algorithm, ML–MOC, developed by Agarwal, Rao & Bhattacharya (2021) on *Gaia* EDR3 data (Gaia Collaboration et al. 2021). The steps followed for determining the members of NGC 2506 using ML–MOC are briefly described here. All the sources with five astrometric parameters (RA, Dec., proper motions in RA, proper motions in Dec., and parallax) and with valid measurements in three *Gaia* photometric passbands G, $G_{\rm BP}$, and $G_{\rm BP}$, were classified as *All sources* if their parallax values were non-negative and the errors in the G magnitudes were smaller than 0.005. From these sources, probable field stars were removed using the k-nearest neighbour (kNN; Cover & Hart 1967) algorithm. These sources with a higher number of cluster members than field stars were termed as *sample sources*. Then the Gaussian mixture model (GMM; Peel & McLachlan 2000) was applied to separate cluster and field members by fitting two

Table 2. The details of *ASTROSAT*/UVIT observations, source detections, and *Gaia* EDR3 counterparts that are identified as members.

Filter name	Exposure time (s)	FWHM (arcsec)	Detections	*Gaia* EDR3 counterparts
F148W (CaF2-1)	9224	1.07	776	464
F154W (BaF2)	7499	1.09	740	438
F169M (Sapphire)	7027	1.11	656	418
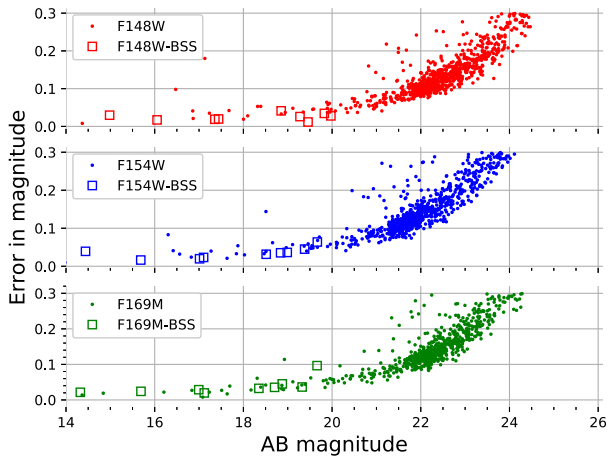
Figure 1. PSF magnitudes versus errors in magnitudes in different UVIT filters. Open squares denote the BSS in respective filters.

Gaussian distributions in the proper motion and parallax space to the *sample sources*. The membership probabilities of all the sources were also assigned using the GMM. We identified 2175 members with $G < 20$ mag within 30 arcmin of the centre of NGC 2506. By cross-matching UVIT-detected sources with these *Gaia* EDR3 members within 1-arcsec search radius using TOPCAT (Taylor 2011), we found counterparts in all the filters. The information on exposure times of observations, the FWHM of sources, the number of detections in all the UVIT filters, and the *Gaia* EDR3 members counterparts are given in Table 2. To identify BSS of NGC 2506, we applied the methodology adopted by Rao et al. (2021) for segregating BSS from MSTO stars and binary stars located above the MSTO. This methodology is briefly summarized as follows. We plotted a PARSEC isochrone (Bressan et al. 2012) with suitable metallicity and age as given in Table 1 to the cluster CMD. We next plotted the equal-mass isochrone to isolate the binary stars. Finally, we selected the stars bluer than this isochrone as BSS. We thus identified nine BSS in this cluster.

3.2 The colour–magnitude diagrams

Fig. 2 shows optical and UV CMDs of the cluster. In the optical CMD, *Gaia* EDR3 members including BSS and sources detected in the UVIT/*F148W* are shown. A PARSEC isochrone[1] (Bressan et al. 2012) of age 2.2 Gyr, distance = 3110 pc, and $Z = 0.0045$ is overplotted after applying extinction correction $A_G = 0.39$ and reddening correction $E(BP - RP) = 0.155$. The age and distance are taken from Vaidya et al. (2020). A binary sequence isochrone is also plotted in the optical CMD for the equal-mass binaries with a G magnitude brighter than 0.75 mag than that of MS stars, as

shown by the pink dashed line. The UV–optical CMD shows all the sources detected in UVIT/*F148W* filter that are also *Gaia* EDR3 members. A BaSTI isochrone[2] (Hidalgo et al. 2018) of the same fundamental parameters after applying extinction correction $A_{F148W} = 0.721$ and reddening correction $E(F148W - G) = 0.473$ has been overplotted. The three YSS candidates detected in UVIT/*F148W* filter are represented by blue open squares, whereas three RC stars are marked as cyan open circles in both optical and UV CMDs. We have also shown the membership probabilities of identified members above $G = 17$ mag according to ML–MOC in both optical and UV CMD. All the BSS, YSS, and RC stars are highly probable members with membership probabilities greater than 0.6 except one RC star (RC3).

We note from the optical CMD that the G-band magnitudes of BSS varies from ~ 0.5 mag below MSTO to $\sim$3 mag above the MSTO. In the UV CMD, the BSS sequence stands out as the *F148W* magnitudes of the BSS vary from $\sim$2 to $\sim$7 mag above the MSTO. We notice a few red giant branch stars brighter than the PARSEC isochrone in the optical CMD, but are not detected in the UV CMD.

3.3 Spectral energy distributions of BSS

The characterization of the BSS and detection of any hot companion associated with them is accomplished by constructing their spectral energy distributions (SEDs). We first examined the images of the BSS in *Aladin*[3] to check if there were any nearby (within 3 arcsec) sources present. We found BSS4 and BSS6 to have multiple sources within 3 arcsec. Moreover, BSS6 is a saturated source. Therefore, these two BSS were excluded from the SED fitting. There is one BSS, BSS9, which is present at the edge of the UVIT image. Its UVIT fluxes may have large errors. However, the *GALEX* FUV and NUV fluxes are available for this source, and hence we include it in the SED fitting. In order to construct SEDs we made use of virtual observatory SED analyser (VOSA; Bayo, Rodrigo & Navascus 2008). Using VOSA, we obtained photometric fluxes of sources in FUV and NUV from *GALEX* (Martin et al. 2005), optical from *Gaia* EDR3 (Gaia Collaboration et al. 2021) and PAN-STARRS (Chambers et al. 2016), near-IR from Two Micron All Sky Survey (2MASS; Cohen, Wheaton & Megeath 2003), and far-IR from *Wide-field Infrared Survey Explorer* (*WISE*; Wright et al. 2010). The photometric fluxes were corrected for extinction by VOSA according to the extinction law by Fitzpatrick (1999) and Indebetouw et al. (2005) using the value of extinction $A_v = 0.248$ provided by us. We obtained this value of average extinction in the cluster from Knudstrup et al. (2020) and Xin & Deng (2005). The values of fluxes of the BSS in different filters are listed in Table 3. VOSA calculates synthetic photometry for selected theoretical models using filter transmission curves and performs a χ^2 minimization test by comparing the

[1] http://stev.oapd.inaf.it/cgi-bin/cmd.

[2] http://basti-iac.oa-abruzzo.inaf.it/hbmodels.html.
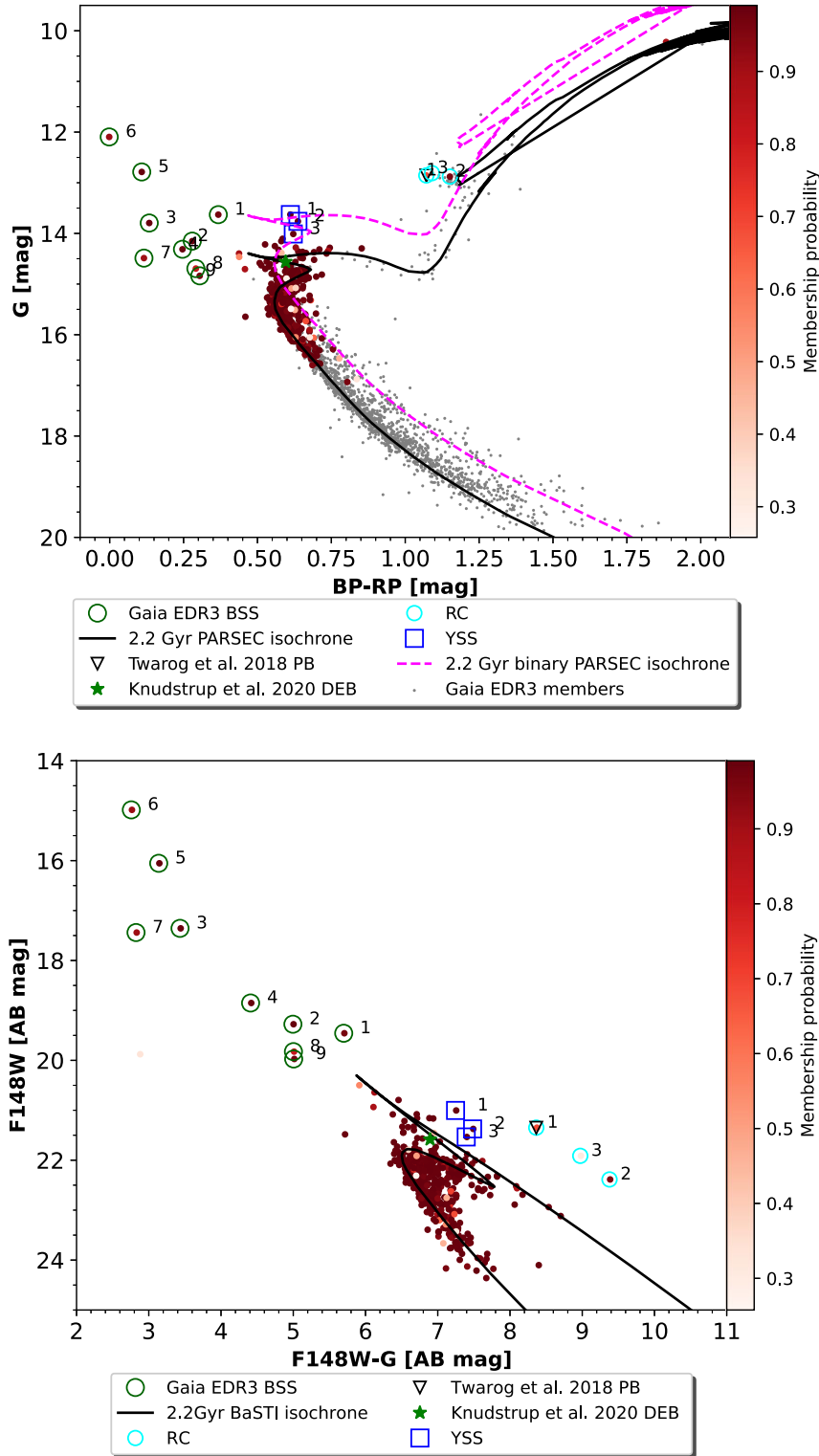[3] https://aladin.u-strasbg.fr/.

Figure 2. The top figure shows the optical CMD of NGC 2506 showing all *Gaia* EDR3 members as grey dots, BSS according to *Gaia* EDR3 members as green open circles (labelled according to the coordinates given in Table 3), *F148W* detections as red dots, YSS detected in all the UVIT filters as blue open squares, a detached eclipsing binary according to Knudstrup et al. (2020) as green star, a probable binary according to Anthony-Twarog et al. (2018) as black open triangle, and RC stars as cyan open circles. A PARSEC isochrone (Bressan et al. 2012) of age = 2.2 Gyr, distance = 3110 pc, and $Z = 0.004$ is plotted after applying the extinction correction of $A_G = 0.39$ and reddening of $E(BP - RP) = 0.155$. A binary sequence isochrone for the equal mass binaries with a G magnitude brighter than 0.75 mag than that of MS is shown in pink dashed line. The bottom figure shows the UV-optical CMD showing all *F148W* detections in red dots. All other sources are represented with the same symbols as in the *Gaia* EDR3 CMD. A BaSTI isochrone (Hidalgo et al. 2018) of the same cluster parameters as the *Gaia* EDR3 CMD has been plotted after applying the extinction correction $A_{F148W} = 0.721$, and reddening correction $E(F148W - G) = 0.473$.

Table 3. Coordinates of all BSS, YSS, and RC stars in Columns 2 and 3, *Gaia* EDR3 ID in Column 4, UVIT *F148W* and *F154W* fluxes in Columns 5 and 6, *GALEX* FUV flux in Column 7, UVIT *F169M* flux in Column 8, *GALEX* NUV flux in Column 9, *Gaia* EDR3 Gbp, G, and Grp fluxes in Columns 10–12, 2MASS *J*, *H*, and K_s fluxes in Columns 13–15, and *WISE* W1, W2, W3, and W4 fluxes in Columns 16–19.

Name / GALEX.FUV±err / PS1.r±err / 2MASS.H±err	RA / UVIT.F169M±err / PS1.i±err / 2MASS.Ks±err	Dec. / GALEX.NUV±err / GAIA3.Grp±err / WISE.W1±err	Gaia EDR3 ID / PS1.g±err / PS1.z±err / WISE.W2±err	UVIT.F148W±err / GAIA3.Gbp±err / PS1.y±err / WISE.W3±err	UVIT.F154W±err / GAIA3.G±err / 2MASS.J±err / WISE.W4±err
BSS1	119.99207	−10.76498	3038044880608396672	1.630e-15 ± 8.654e-19	2.110e-15 ± 4.692e-18
–	2.050e-15 ± 5.585e-18	–	1.988e-14 ± 4.604e-17	1.636e-14 ± 5.059e-17	1.079e-14 ± 2.799e-17
1.150e-14 ± 1.021e-17	6.975e-15 ± 1.596e-17	6.416e-15 ± 2.300e-17	4.800e-15 ± 3.276e-18	3.880e-15 ± 1.548e-17	1.837e-15 ± 4.398e-17
7.371e-16 ± 2.037e-17	2.848e-16 ± 7.871e-18	5.504e-17 ± 1.267e-18	1.407e-17 ± 3.759e-19	–	–
BSS2	119.99902	−10.75405	3038046358077125248	1.927e-15 ± 2.721e-18	2.424e-15 ± 6.079e-18
–	2.406e-15 ± 6.101e-18	–	1.272e-14 ± 5.119e-17	1.042e-14 ± 2.818e-17	6.667e-15 ± 1.729e-17
7.054e-15 ± 8.083e-18	4.129e-15 ± 5.099e-18	3.769e-15 ± 1.344e-17	2.780e-15 ± 3.687e-18	2.242e-15 ± 5.599e-18	1.081e-15 ± 2.988e-17
4.065e-16 ± 1.573e-17	1.512e-16 ± 7.796e-18	–	–	–	–
BSS3	119.97925	−10.79276	3038044674450004736	1.159e-14 ± 7.939e-17	1.339e-14 ± 1.143e-16
–	1.184e-14 ± 1.321e-16	–	1.868e-14 ± 6.800e-17	1.518e-14 ± 4.195e-17	9.267e-15 ± 2.393e-17
9.544e-15 ± 3.118e-17	5.226e-15 ± 6.397e-18	4.800e-15 ± 1.740e-17	3.433e-15 ± 1.333e-17	2.730e-15 ± 7.651e-18	1.191e-15 ± 3.072e-17
4.429e-16 ± 1.509e-17	1.623e-16 ± 7.323e-18	3.277e-17 ± 7.546e-19	8.574e-18 ± 2.922e-19	–	–
BSS4	120.00583	−10.73528	3038046598595270656	2.857e-15 ± 9.692e-18	3.277e-15 ± 1.009e-17
–	3.339e-15 ± 1.101e-17	–	9.181e-15 ± 2.852e-17	1.129e-14 ± 3.774e-17	5.751e-15 ± 1.504e-17
3.220e-15 ± 1.579e-17	6.147e-15 ± 5.735e-18	3.479e-15 ± 5.793e-18	8.574e-16 ± 2.685e-17	2.328e-15 ± 7.469e-18	1.861e-15 ± 4.151e-18
3.229e-16 ± 1.309e-17	1.267e-16 ± 7.816e-18	2.728e-17 ± 1.457e-18	7.413e-18 ± 4.506e-19	–	–
BSS5	120.02733	−10.81018	3038043746737021440	4.175e-14 ± 1.015e-15	4.946e-14 ± 1.408e-15
3.896e-14 ± 7.237e-16	4.165e-14 ± 1.487e-15	4.595e-14 ± 3.330e-16	–	3.892e-14 ± 1.026e-16	2.345e-14 ± 5.981e-17
–	–	1.202e-14 ± 4.229e-17	8.603e-15 ± 2.248e-17	6.918e-15 ± 2.697e-17	3.059e-15 ± 6.762e-17
1.078e-15 ± 2.582e-17	3.943e-16 ± 1.126e-17	8.501e-17 ± 1.801e-18	2.282e-17 ± 5.045e-19	6.693e-19 ± 2.700e-19	–
BSS6	120.03826	−10.80378	3038043776795821312	1.461e-13 ± 2.300e-14	2.274e-13 ± 7.734e-14
1.979e-13 ± 1.604e-15	1.953e-13 ± 3.180e-14	1.340e-13 ± 5.6e-16	–	7.654e-14 ± 2.018e-16	4.431e-14 ± 1.130e-16
–	–	2.134e-14 ± 7.460e-17	–	1.169e-14 ± 1.663e-17	4.989e-15 ± 1.103e-16
1.747e-15 ± 4.184e-17	6.69e-16 ± 1.725e-17	–	–	–	–
BSS7	119.98425	−10.69498	3038058590143955968	1.070e-14 ± 7.041e-17	1.228e-14 ± 1.128e-16
9.437e-15 ± 3.583e-16	1.053e-14 ± 7.115e-17	1.102e-14 ± 1.656e-16	1.008e-14 ± 4.276e-17	8.059e-15 ± 2.262e-17	4.895e-15 ± 1.291e-17
5.029e-15 ± 8.755e-18	2.733e-15 ± 4.056	2.507e-15 ± 9.180e-18	1.789e-15 ± 4.141e-18	1.423e-15 ± 3.327e-18	5.867e-16 ± 1.729e-17
2.128e-16 ± 9.210e-18	8.658e-17 ± 6.619e-18	1.573e-17 ± 4.201e-19	4.413e-18 ± 1.951e-19	–	–
BSS8	120.11296	−10.76647	3038042784664224000	1.160e-15 ± 1.270e-18	1.468e-15 ± 2.758e-18
7.909e-16 ± 1.084e-16	1.355e-15 ± 1.924e-18	3.641e-15 ± 9.689e-17	7.747e-15 ± 2.445e-17	6.288e-15 ± 1.758e-17	4.049e-15 ± 1.048e-17
4.363e-15 ± 7.433e-18	2.529e-15 ± 3.498e-28	2.299e-15 ± 8.198e-18	1.694e-15 ± 2.030e-18	1.369e-154 ± 5.803e-18	6.020e-16 ± 1.830e-17
2.284e-16 ± 1.073e-17	8.674e-17 ± 7.350e-18	1.636e-17 ± 4.220e-19	4.226e-18 ± 1.946e-19	–	–

Table 3 – *continued*

Name / GALEX.FUV±err / PS1.r±err / 2MASS.H±err	RA / UVIT.F169M±err / PS1.i±err / 2MASS.Ks±err	Dec. / GALEX.NUV±err / GAIA3.Grp±err / WISE.W1±err	Gaia EDR3 ID / PS1.g±err / PS1.z±err / WISE.W2±err	UVIT.F148W±err / GAIA3.Gbp±err / PS1.y±err / WISE.W3±err	UVIT.F154W±err / GAIA3.G±err / 2MASS.J±err / WISE.W4±err
BSS9	119.77495	−10.86142	3038049862770680832	1.012e-15 ± 7.767e-19	1.127e-15 ± 2.263e-18
7.742e-16 ± 1.133e-16	9.929e-16 ± 2.684e-18	2.753e-15 ± 8.276e-17	6.78-e15 ± 1.025e-17	5.488e-15 ± 1.677e-17	3.547e-15 ± 9.140e-18
3.843e-15 ± 8.456e-18	2.243e-15 ± 2.852e-18	2.031e-15 ± 7.321e-18	1.504e-15 ± 2.040e-18	1.215e-15 ± 2.406e-18	5.326e-16 ± 1.423e-17
2.060e-16 ± 1.120e-17	7.109e-17 ± 7.595e-18	1.503e-17 ± 4.016e-19	4.725e-18 ± 1.828e-19	1.437e-18 ± 2.314e-19	1.116e-18 ± 1.796e-19
–	120.00234	−10.76055		3.911e-16 ± 2.094e-19	4.740e-164 ± 5.680e-19
1.201e-14 ± 7.178e-18	3.392e-16 ± 2.668e-19	7.366e-15 ± 2.603e-17	1.735e-14 ± 4.975e-17	1.500e-144 ± 4.041e-17	1.081e-14 ± 2.753e-17
1.061e-15 ± 2.835e-17	7.942e-15 ± 3.632e-17	5.794e-15 ± 5.091e-18	—	4.662e-15 ± 1.278e-17	2.450e-15 ± 5.190e-17
	4.175e-16 ± 1.153e-17	8.346e-17 ± 1.922e-18	2.274e-17 ± 6.074e-19	—	—
–	120.02626	−10.77780		2.780e-16 ± 1.764e-19	3.500e-16 ± 3.048e-19
1.073e-14 ± 1.797e-17	1.762e-16 ± 6.640e-20	6.623e-15 ± 2.349e-17	1.498e-14 ± 3.374e-17	1.318e-14 ± 3.581e-17	9.553e-15 2.438e-17
	7.207e-15 1.707e-17	5.169e-15 ± 1.527e-17		4.299e-15 ± 4.930e-18	2.280e-15 ± 6.091e-17
9.788e-16 ± 2.795e-17	3.623e-16 ± 1.368e-17	8.194e-17 ± 3.321e-18	2.370e-17 ± 9.823e-19	1.407e-18 ± 3.409e-19	—
–	120.01897	−10.80028		2.397e-16 ± 1.128e-19	3.025e-16 ± 2.356e-19
8.416e-15 ± 3.031e-17	1.798e-16 ± 9.825e-20	5.205e-15 ± 1.853e-17	1.212e-14 ± 2.791e-17	1.051e-14 ± 2.863e-17	7.591e-15 ± 1.936e-17
7.337e-16 ± 1.960e-17	5.674e-15 ± 4.949e-18	4.098e-15 ± 8.572e-18	—	3.322e-15 ± 6.094e-18	1.743e-15 ± 4.334e-17
	2.766e-16 ± 1.095e-17	5.545e-17 ± 1.175e-18	1.575e-17 ± 3.771e-19	—	—
–	119.97858	−10.7792		2.845e-16 ± 1.378e-19	3.414e-16 ± 2.410e-19
—	1.772e-16 ± 6.958e-20	1.870e-14 ± 6.577e-17	—	2.494e-14 ± 6.525e-17	2.201e-14 ± 5.601e-17
—	—	—	—	—	8.987e-15 ± 1.904e-16
5.127e-15 ± 1.228e-16	2.098e-15 ± 4.444e-17	4.332e-16 ± 9.576e-18	1.246e-16 ± 2.525e-18	3.641e-18 ± 3.186e-19	—
–	119.924610	−10.72398		1.094e-16 ± 3.214e-20	1.324e-16 ± 5.066e-20
—	8.247e-17 ± 2.659e-20	1.896e-14 ± 6.636e-17	—	22.348e-14 ± 6.186e-17	2.155e-14 ± 5.479e-17
—	—	—	—	—	9.341e-15 ± 1.979e-16
5.104e-15 ± 1.222e-16	2.213e-15 ± 4.281e-17	4.524e-16 ± 9.583e-18	1.246e-16 ± 2.295e-18	3.743e-18 ± 2.827e-19	—
–	120.05109	−10.81254		1.692e-16 ± 5.877e-20	2.280e-16 ± 1.358e-19
2.417e-14 ± 0.000e+00	1.253e-16 ± 4.726e-20	1.965e-14 ± 6.899e-17	2.681e-14 ± 4.340e-17	2.574e-14 ± 6.696e-17	2.294e-14 ± 5.836e-17
1.998e-14 ± 0.000e+00	1.998e-14 ± 0.000e+00	—	1.658e-14 ± 0.000e+00	1.417e-14 ± 7.838e-17	9.410e-15 ± 1.907e-16
5.194e-15 ± 1.005e-16	2.052e-15 ± 4.158e-17	4.195e-16 ± 8.886e-18	1.145e-16 ± 2.109e-18	3.581e-18 ± 2.671e-19	—

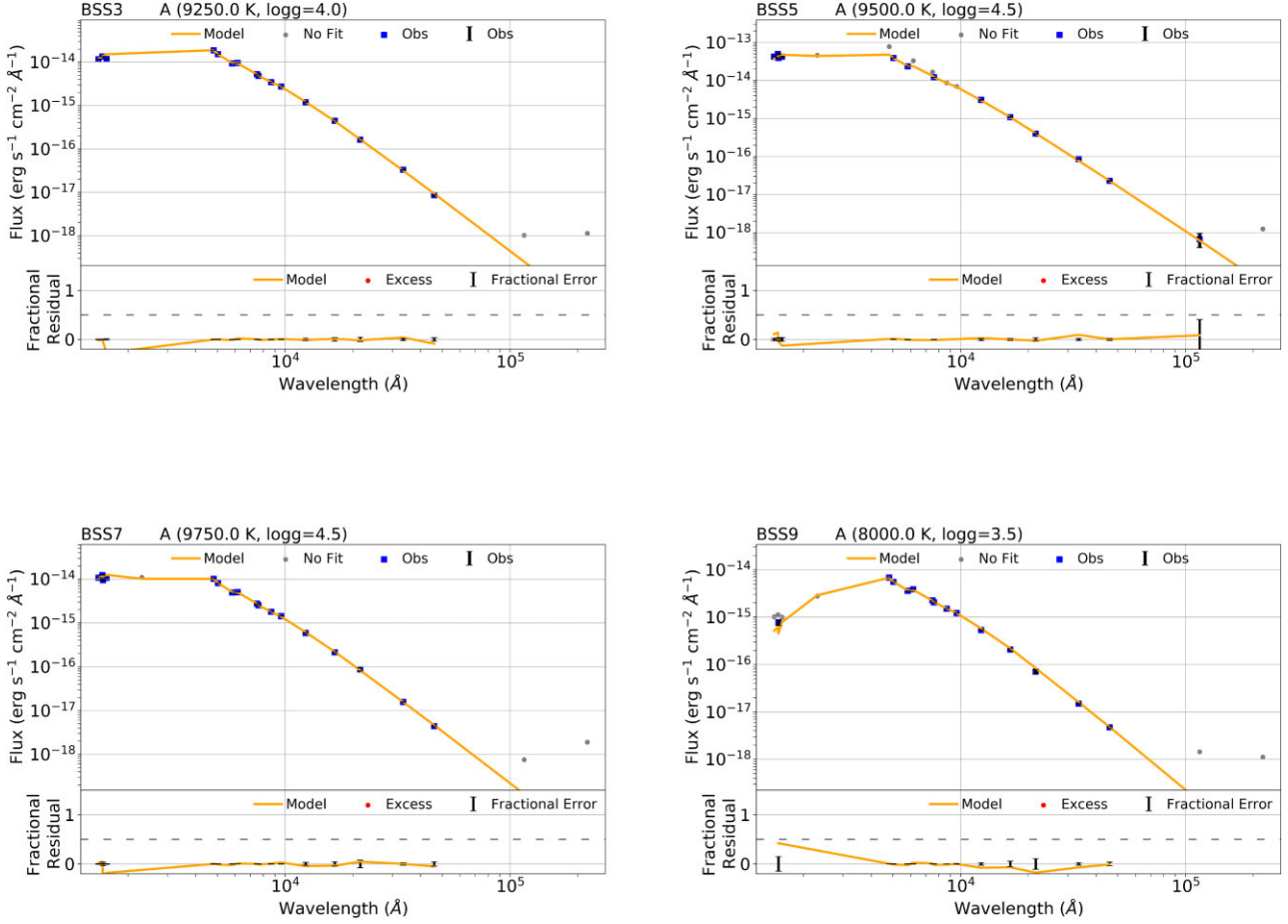*Note.* All flux values are listed in the unit of erg s^{-1} cm^{-2} Å^{-1}.

Figure 3. The single-component SED fits of BSS. In the top panel, blue data points show the extinction corrected observed fluxes, with black error bars representing the errors in observed fluxes, and the orange curve representing the Kurucz stellar model fit. The bottom panel shows the residual between extinction-corrected observed fluxes and the model fluxes across the filters from UV to IR wavelengths.

synthetic photometry with the extinction-corrected observed fluxes to get the best-fitting parameters of the SED. The reduced χ_r^2 is determined using the following formula:

$$\chi_r^2 = \frac{1}{N - N_f} \sum_{i=1}^{N} \frac{(F_{o,i} - M_d F_{m,i})^2}{\sigma_{o,i}^2}, \qquad (1)$$

where N is the number of photometric data points used and N_f is the number of free parameters in the model. $F_{o,i}$ and $F_{m,i}$ are the observed and the model flux of the star, respectively. M_d is the scaling factor by which the model is to be multiplied to get the fit and is given by $(R/D)^2$, where R is the radius of the star, D is the distance to the star, and $\sigma_{o,i}$ is the error in the observed flux.

In order to fit the SEDs to the BSS, we used the Kurucz stellar models (Castelli, Gratton & Kurucz 1997). We kept $T_{\rm eff}$ and log g as free parameters and chose their ranges to be 3500–50000 K and 3–5, respectively. We fixed the value of metallicity ([Fe/H]) to be −0.5, which is the nearest to the cluster metallicity −0.36 (Knudstrup et al. 2020). While fitting the SEDs, we first excluded the UV data points from the SEDs and confirmed whether optical and IR data points were fitting satisfactorily with the model flux. We checked carefully if excess to the UV and/or IR data points were present and also noted the residuals (the difference between model flux and the observed flux) in all the UV filters. Out of seven BSS, four showed fractional residual less than 0.3 in all the UV data points, and therefore we fitted them with single-component SEDs. Fig. 3 shows

all the single-component SEDs. The top panel for each BSS shows the fitted SED of each BSS where blue data points are the extinction-corrected observed fluxes with error bars shown in black, and the orange curve is the model fit. The bottom panel shows the residual between observed fluxes and the model fluxes in each filter. In BSS5, BSS7, and BSS9, fluxes were available in both *GALEX*/FUV and *GALEX*/NUV filters. However, *GALEX*/NUV points were flagged as bad in the *GALEX* catalogue (Bianchi et al. 2000) itself, hence we did not use them in the fitting. As mentioned above, since BSS9 is located at the edge of the UVIT image, UVIT data points of this BSS are excluded from the SED fitting. In BSS3, BSS7, and BSS9, the upper limits were available for both *WISE* W3 and W4, whereas in the case of the BSS5, the upper limit was available in the *WISE* W4 filter. Hence, these data points are excluded from the corresponding SEDs of BSS. We note that for these BSS (BSS3, BSS5, BSS7, and BSS9), the residuals are coming out to be nearly zero, indicating that the extinction-corrected observed fluxes and the model fluxes in all filters are comparable. The satisfactory fitting of the single-component SED suggests that there are no signatures of the presence of any hotter companions associated with these four BSS.

The parameters of all the BSS obtained from double-component SEDs, are listed in Table 4. The χ^2 of the fits are large even when the SED fits are visually good due to some data points with very small observational flux errors (Rebassa-Mansergas et al. 2021). In view of this fact, VOSA also determines another parameter called visual

Table 4. The best-fitting SED parameters of BSS, YSS, and RC stars and their hot companions.

Name	Component	log g	Luminosity (L$_\odot$)	T_{eff} (K)	Radius (R$_\odot$)	χ_r^2 ($\chi_{r,single}^2$)	Scaling factor	N_{fit}	vgf$_b$ (vgf$_{b,single}$)
BSS1	A	3.5	31.18 ± 9.05	7750 ± 125	3.10 ± 0.44	308.06 (649)	5.06E-22	16	0.15 (0.25)
	B	7.5	$0.44^{+0.22}_{-0.19}$	13 250 ± 250	0.13±+0.02	–	8.24E-25	–	
BSS2	A	3.0	19.30 ± 5.60	8000 ± 125	2.29 ± 0.33	266.26 (694)	2.77E-22	14	0.03 (0.16)
	B	8.0	$0.45^{+0.23}_{-0.20}$	15 000 ± 250	0.10 ± 0.01	–	5.21E-25	–	
BSS3	Single	4.0	31.58 ± 9.16	9250 ± 125	2.19 ± 0.31	48.32	2.53E-22	18	0.58
BSS5	Single	4.5	84.37 ± 24.49	9500 ± 125	3.38 ± 0.49	13.26	6.03E-22	14	0.54
BSS7	Single	4.5	18.40 ± 5.34	9750 ± 125	1.51 ± 0.21	68.83	1.21E-22	17	0.57
BSS8	A	3.0	12.06 ± 3.50	8250 ± 125	1.70 ± 0.24	596.22(1864)	1.52E-22	18	0.91 (1.51)
	B	7.5	$0.24^{+0.12}_{-0.11}$	19 000 ± 250	0.05 ± 0.01	–	1.19E-25	–	
BSS9	Single	3.0	10.58 ± 3.07	8250 ± 125	1.60 ± 0.23	2389	1.35E-22	16	1.59
YSS1	A	3.5	30.73 ± 8.92	6750 ± 125	4.06 ± 0.58	17.88 (4771)	8.69E-22	16	0.04(2.09)
	B	4.5	$0.14^{+0.08}_{-0.07}$	29 000 ± 1000	0.01 ± 0.00	–	1.15E-26	–	
YSS2	Single	3.0	26.72 ± 7.77	6500 ± 125	4.08 ± 0.59	29.39	8.77E-22	17	0.66
YSS3	A	3.5	21.84 ± 6.34	6750 ± 125	3.42 ± 0.49	15.31 (33 835)	6.16E-22	16	0.10 (2.13)
	B	3.5	$0.07^{+0.04}_{-0.03}$	26 000 ± 1000	0.01 ± 0.00	–	8.48E-27	–	
RC1	A	4.0	67.49 ± 19.67	5250 ± 125	9.86 ± 1.42	28.12 (1140)	5.11E-21	13	3.07 (91)
	B	5.0	$0.13^{+0.08}_{-0.06}$	3 0000 ± 1000	0.01 ± 0.00	–	9.39E-27	–	
RC2	A	3.5	67.54 ± 19.69	5000 ± 125	10.96 ± 1.58	71.5 (517 632)	6.31E-21	13	0.25 (0.99)
	B	5.0	$0.05^{+0.03}_{-0.02}$	25 000 ± 1000	0.01 ± 0.00	–	8.48E-27	–	
RC3	A	5.0	69.30 ± 20.42	5250 ± 125	10.04 ± 1.45	17.88 (26 880)	5.29E-21	18	0.04(1.33)
	B	5.0	$0.09^{+0.05}_{-0.04}$	31 000 ± 1000	0.01 ± 0.00	–	5.64E-27	–	

Notes. For each of them, whether the single- or double-component SED is satisfactory in Column 2, log g in Column 3, luminosity, temperature, and radius in Columns 4–6, the reduced χ_r^2 values in Column 7 (in case of double-component fits, the χ_r^2 values of the single fits are given in the brackets), scaling factor in Column 8, number of data points used to fit the SED is given in Column 9, and the values of vgf$_b$ parameter in Column 10 (in case of double-component fits, the vgf$_b$ values of the single fits are given in the brackets).

goodness of fit (vgf$_b$). It is a modified reduced χ^2, which is calculated by forcing the observational errors to be at least 10 per cent of the observed flux. It is determined using the following formula:

$$\text{vgf}_b = \frac{1}{N - N_f} \sum_{i=1}^{N} \frac{(F_{o,i} - M_d F_{m,i})^2}{b_i^2}, \tag{2}$$

where $\sigma_{o,i} \leq 0.1F_{o,i} \Rightarrow b_i = 0.1F_{o,i}$ and $\sigma_{o,i} \geq 0.1F_{o,i} \Rightarrow b_i = \sigma_{o,i}$. We note that the values of vgf$_b$ parameters are < 2 for all single- and double-component SEDs. These fits are acceptable since the value of vgf$_b < 15$ is an indicative of good SED fits (Jiménez-Esteban et al. 2018; Rebassa-Mansergas et al. 2021).

Three BSS (BSS1, BSS2, and BSS8) show fractional residual greater than 0.3 in the UV data points. Therefore, these three BSS are fitted with a double component using a PYTHON code, BINARY SED FITTING,[4] by Jadhav et al. (2021b), which is based on χ_r^2 minimization technique to fit the double-component SEDs. To fit the hotter component, we used the Koester model (Koester 2010), since this model gives a temperature range of 5000–8 0000 K and log g range of 6.5–9.5. Fig. 4 shows the double-component SEDs for BSS1, BSS2, and BSS8. For each BSS, the top panel shows the fitted SED, and the bottom panel shows the residual for single and composite fit in every filter. The composite fit satisfactorily takes care of the excess in the UV data points and the residual turns out to be nearly zero in all the data points, which is reflecting in the significantly lower

χ_r^2 values of the double fit as listed in Table 4. For these BSS, the parameters of the cooler components are taken from VOSA, whereas the parameters of the hotter companions are taken from BINARY SED FITTING, by Jadhav et al. (2021b). In order to determine the errors in the parameters of hot companions, we have followed the statistical approach as described in Jadhav et al. (2021a). For this, we generated 100 iterations of observed SEDs for each BSS by adding Gaussian noise, proportional to the errors, to each data point. We fitted these 100 SEDs using the Koester model as described earlier, and derived the parameters of the hotter companions based on these SED fittings. We considered the median values of the parameters derived from the 100 SEDs to be the parameters of hot companions, whereas, for the errors in the parameters, we considered the standard deviation from the median parameters. If the statistical error is less than the step size of stellar models, half of the step size (e.g. 250 K for the Kurucz model) is taken as temperature error.

3.4 SEDs of YSS and RC stars

We also constructed the SEDs for the three YSS and three RC candidates detected in all UVIT/FUV filters using VOSA, following the same steps as described for BSS using Kurucz model (Castelli et al. 1997). All these six sources showed excess in UV data points, suggesting the presence of hot companions. In all the cases, composite fit has reduced χ^2 of the fit significantly compared to single fits, except YSS2 for which no satisfactory double fit was found. Therefore, only the single-component SED has been shown

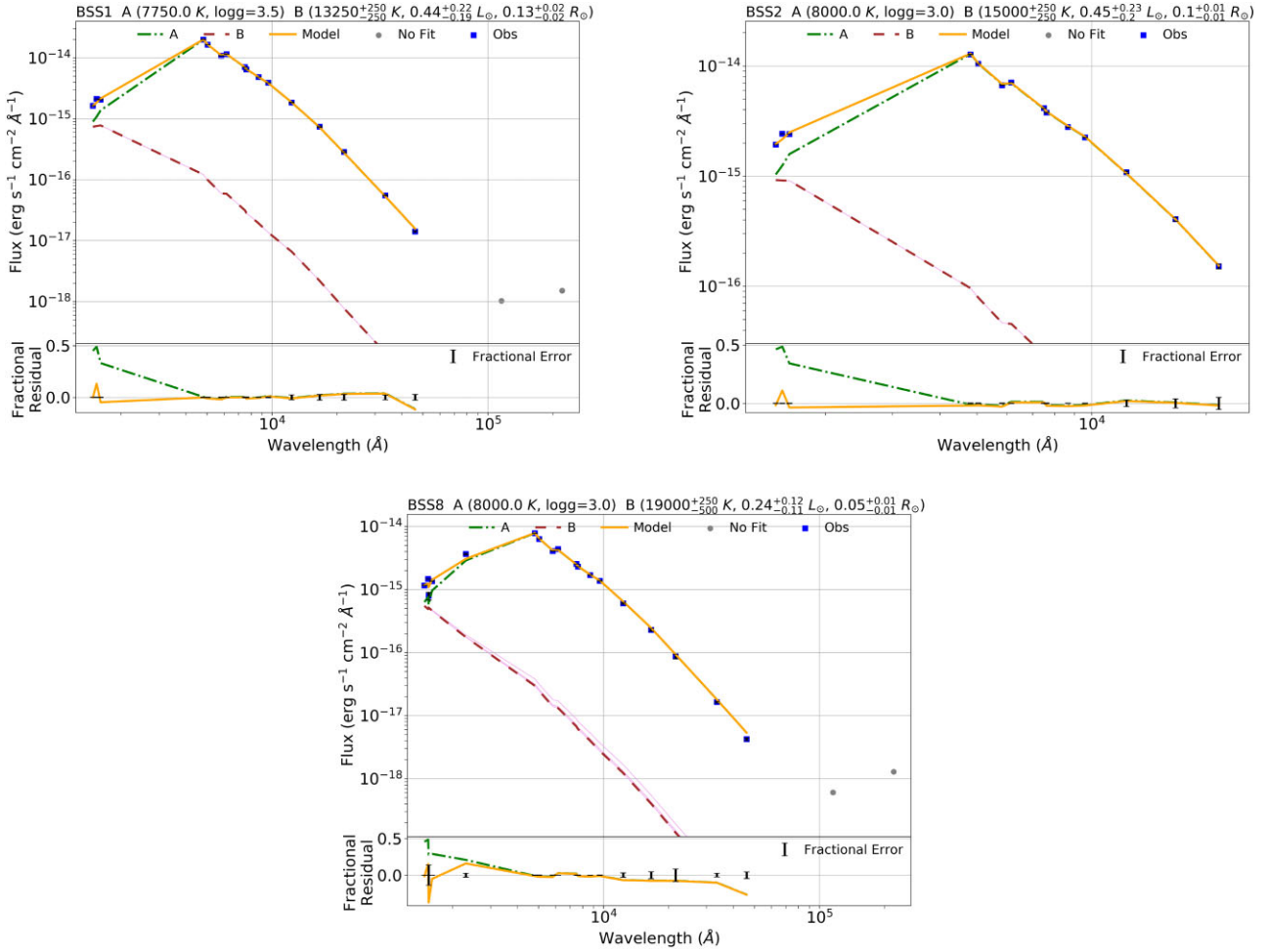[4]https://github.com/jikrant3/Binary SED Fitting.

Figure 4. The binary component fit SEDs of BSS. The top panel shows the double-component SED of each BSS where blue data points are the extinction corrected flux values with flux errors as black error bars. The green dashed line is the cool (A) component fit, and the brown dashed line is the hot (B) component fit with pink curves denoting the residual of iterations. The composite fit is shown in orange curve and the data points that are not included in the fits are denoted by grey data points. The bottom panel shows the fractional residual for both single (green) and composite (orange) fits. The fractional errors are shown on the *x*-axis by black error bars. The parameters of the cool and hot components that were derived from the SEDs along with the estimated errors are mentioned at the top of the plots.

for YSS2. The SEDs of YSS and RC stars are shown in Fig. 5 and their estimated parameters are tabulated in Table 4. We also fitted the primary component of our objects (BSS, YSS, and RC stars) with Coelho synthetic stellar library (Coelho 2014). We found that sources with UV excess in the Kurucz stellar models also showed similar UV excess when fitted with the Coelho model. This implies that the residuals in the UV data points are independent of the stellar models used. However, in this work, we have presented the results of SED fits using the Kurucz model.

4 DISCUSSIONS

4.1 BSS, YSS, and RC star properties

As mentioned above, on fitting the SEDs, we obtain the parameters such as temperatures, radii, and luminosities of BSS, YSS, and RC stars as well as their hotter components. The hot temperatures (7750–9750 K) of NGC 2506 BSS are consistent with the young age (2.2 Gyr) of the cluster. This temperature range of BSS is comparable to temperatures of the BSS of other intermediate-age

OCs such as NGC 7789 that varies from 7250 to 10 250 K (Vaidya et al. 2022) and NGC M67 having a temperature range of 6250–9000 K (Sindhu et al. 2019; Pandey et al. 2021). We note that from the SEDs, that the temperatures of YSS varies from 6500 to 6750 K. This shows that YSS are cooler than BSS, which is expected since the YSS are presumably evolved BSS. Moreover, RC stars have temperature that varies from 5000 to 5250 K. We compared the SED-based temperatures of our objects (BSS, YSS, and RCs) with the BP/RP spectra-based temperatures from *Gaia* DR3 (Babusiaux et al. 2022; De Angeli et al. 2022). Our SED-estimated temperatures match *Gaia* DR3 temperatures to within 400 K for objects that have single-temperature fits, but vary greatly in objects found with hot companions. This is not surprising as the spectrophotometric parameters are not likely to be accurate in case of binaries.

We made a comparison with ZAMS and found that all BSS have masses of 1.61–2.16 $M_\odot$. On comparing with the turn-off mass, 1.45 $M_\odot$ of the cluster, we suggest that these BSS must have at least gained ~ 0.16–0.71 $M_\odot$ through the mass transfer process.

We checked for the information on variability of BSS, YSS, and RC stars in *Gaia* DR3. Two of our objects, BSS1 and YSS1,
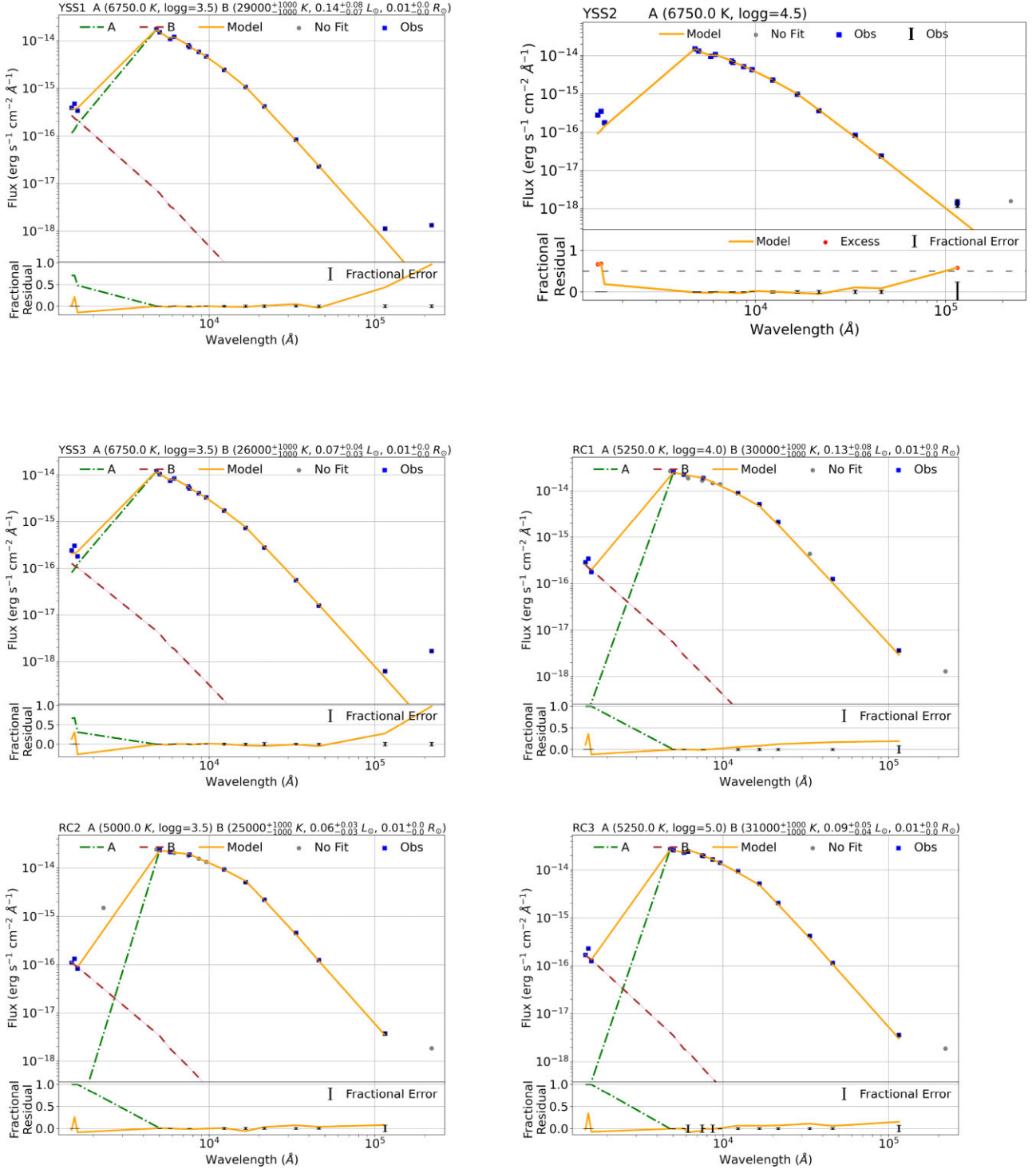
Figure 5. SEDs of YSS and RC stars. The symbols and curves mean the same as in Fig. 3.

are found to be short time-scale (< 0.5–1 d) MS-type oscillators (GDOR|DSCTU|SXPHE).

4.2 The nature of hot companions

We plot the H-R diagram as shown in Fig. 6 to understand the nature of the hot companions of the BSS, YSS, and RC stars. The upper panel of this diagram includes a PARSEC isochrone of age $= 2.2$ Gyr,

distance $= 3110$ pc, $Z = 0.0045$, and a zero-age main sequence (ZAMS). We have shown the cooler as well as hotter companions of BSS, YSS, and RCs of NGC 2506 along with the hot companions of BSS of other OCs. We notice that the single SED fitted BSS are bluer than the A-component of the double temperature fitted BSS. As mentioned earlier, the YSS (both single and double SED fitted) are brighter than the subgiant branch and cooler than the BSS. It is interesting to note three sequences of single BSS, binary BSS, and YSS in
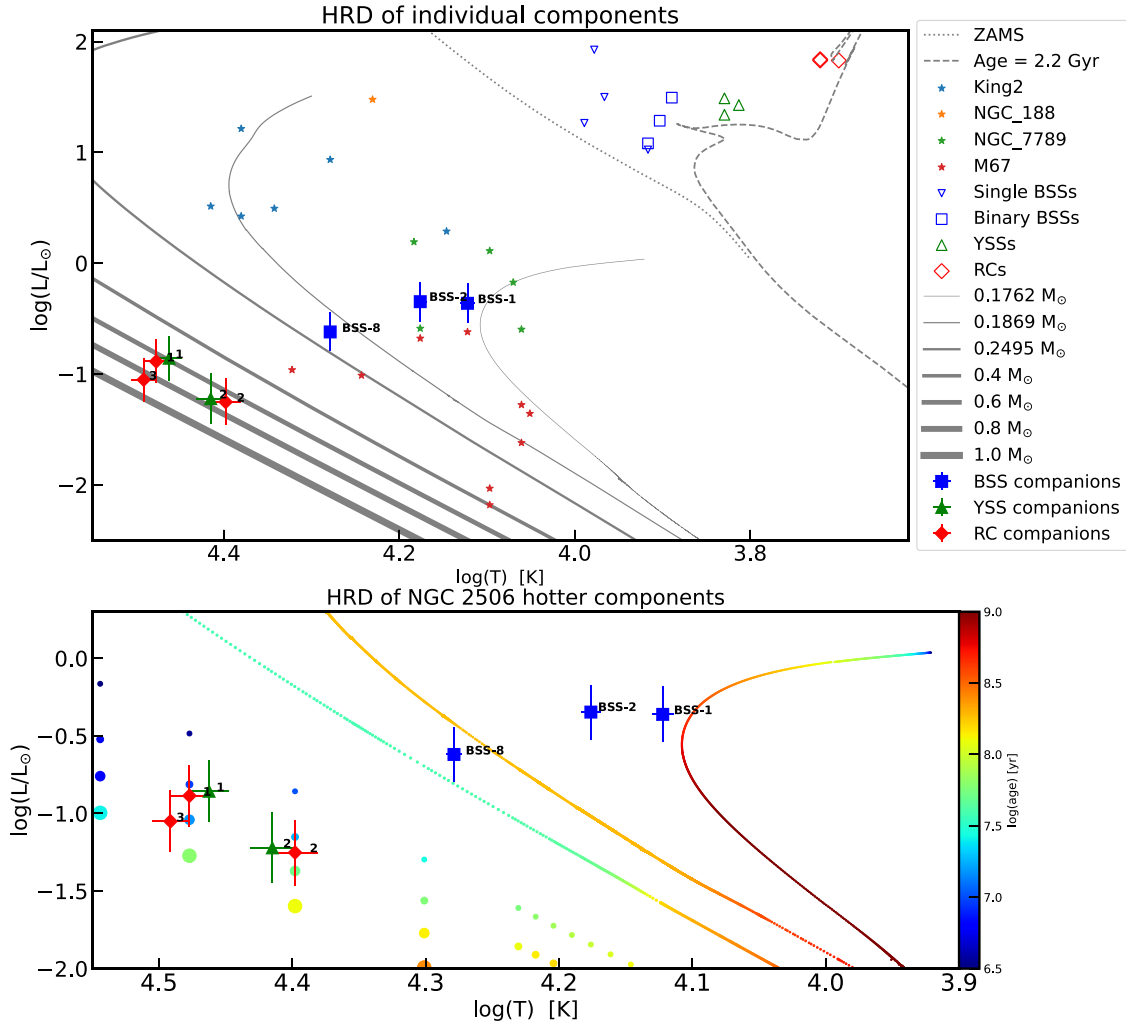
Figure 6. The upper panel represents the H-R diagram showing the single-component BSS as blue open triangles, the cooler component BSS as blue open squares, and their corresponding hotter companions as blue filled squares. Hotter companions of RC stars and YSS are denoted by red diamonds and green triangles, respectively. Their corresponding cooler components are denoted by open diamonds and triangles of the same colours. Hotter companions of BSS of other OCs are shown in different symbols. A PARSEC isochrone of age 2.2 Gyr is plotted as the grey dotted curve and ZAMS is plotted as the grey dashed curve. LM and ELM WD cooling curves of different masses taken from Panei et al. (2007) and Althaus, Bertolami & Córsico (2013), respectively, are represented by different solid grey curves. The lower panel shows the hot companions of NGC 2506 lying on the LM and ELM WD cooling curves of different masses taken from Panei et al. (2007) and Althaus et al. (2013), respectively, indicating their approximate cooling ages.

the H-R diagram from hotter to cooler temperatures. RC1-A, RC2-A, and RC3-A lie on the location of the RC stars in the H-R diagram.

Among the hot companions of BSS, BSS8-B lies on the WD cooling curve of mass $0.20\,M_\odot$ (Panei et al. 2007), suggesting it to be a low-mass (LM) WD. The locations of BSS1-B and BSS2-B in the H-R diagram suggest them to be extremely low mass (ELM) WDs since they are lying very close to the ELM WD cooling curves (Althaus et al. 2013) of masses 0.17 and $0.18\,M_\odot$, respectively. ELM WDs are the stellar remnants that do not ignite helium in their cores (Brown et al. 2010). The detection of LM/ELM WD companion supports the Case A/Case B mass transfer formation mechanism of BSS because the LM WDs (masses $< 0.4\,M_\odot$) and ELM WDs (masses $< 0.2\,M_\odot$) cannot form from a single star evolution within Hubble time (Brown et al. 2011). This implies that these WDs must have undergone mass-loss during their evolution. The location of NGC 2506 BSS hot companions in the H-R diagram is similar to the hot companions of BSS in other intermediate-age OCs such as M67

(Sindhu et al. 2019) and NGC 7789 (Vaidya et al. 2022) that also show LM/ELM WDs candidates for some of their BSS.

The hot companions of RC1 and RC2 lie on the Bergeron WD model of mass $\sim 0.6\,M_\odot$, whereas that of RC3 lies on the Bergeron WD model of mass $\sim 0.8\,M_\odot$. It can be noted that the hot companion of YSS1 and YSS3 also lie on the Bergeron WD model of masses ~ 0.6 and $\sim 0.8\,M_\odot$, respectively. The hot companions of the two YSS and three RC stars are hotter and less luminous than the above hot companions of BSS. The lower panel of Fig. 6 shows the approximate ages of the hot companions of BSS according to Panei et al. (2007) and Althaus et al. (2013) models and that of RC stars and YSS according to the Bergeron WD models (Tremblay & Bergeron 2009). It can be inferred that the hot companions of BSS have log age of ~ 7.5–8.5, hot companions of YSS have log age of ~ 7.0–8.0, and log age of hot companions of RC stars varies from ~ 6.5 to 7.5.

It is noteworthy that radial velocity (RV) for these three RC sources are available in *Gaia* DR2. Their RVs are found as RC1

$= 79.98 \pm 2.13$, RC2 $= 93.79 \pm 1.60$, and RC3 $= 82.19 \pm 1.73$ km s^{-1}. These values are consistent with the cluster mean RV, 84 km s^{-1}, and therefore these RCs should indeed be the members of the cluster. Moreover, RC1 is a probable binary according to the spectroscopic study by Anthony-Twarog et al. (2018) where they have reported its RV to be 82.1 km s^{-1}.

In the absence of comprehensive RV studies, for most cluster sources, their spectroscopic binary fraction are not known. The binarity information of our sources (BSS, YSS, and RC stars) is not available in *Gaia* DR3 (Eyer et al. 2022). From our SED analysis, we find that at least three out of seven (42 per cent) BSS in this cluster are formed through the mass transfer. We also find two out of three YSS in this cluster to be binaries. Among the BSS + YSS population, the binary fraction is 50 per cent, suggesting a significant pathway of formation through mass transfer. The above estimations provide a lower limit, as they are based on systems with detectable hot companions. Recently, a 1.6-Gyr-old cluster, NGC 7789, was found to have at least 33 per cent of the BSS to have formed via mass transfer (Vaidya et al. 2020).

The detected hot companions to the BSS/YSS/RCs show a large spread in mass and age. The mass range covers low- to high-mass WDs (0.2–0.8 M$_\odot$), whereas the turn-off star of this cluster will evolve to an ~ 0.6-M$_\odot$ WD. The presence of LM WDs suggest the existence of Case A/B mass transfer among close binary systems. The three systems (two RCs and one YSS) with a normal mass (~ 0.6 M$_\odot$) WD can be formed through the evolution of a normal turn-off star of mass 1.45 M$_\odot$. In these systems, mass transfer may or may not have happened as it will depend on the binary period. However, the presence of high-mass (> 0.6 M$_\odot$) WDs in two systems (YSS3 and RC3) suggests that the progenitors were massive than turn-off stars, likely BSS, demanding that the progenitors need to be higher order systems. We detect two such systems (YSS3 and RC3) that should have been at least triples. Knudstrup et al. (2020) studied three detached eclipsing binaries in this cluster. They classified one among these three to be a likely triple system that is also detected in the UVIT/FUV images. Their detailed analysis suggested an inner close binary (1.47 and 1.25 M$_\odot$) of an ~ 2.9-d period with a likely ~ 0.7-M$_\odot$ star in an eccentric large (~ 443 d) orbit that could either be a WD or an MS star. Therefore, at least one triple system with close inner binary is present in the cluster. It is quite possible that similar systems could be the progenitors of YSS3 and RC3. These two systems suggest that the BSS formation pathway through triple systems are indeed operational in this cluster. More importantly, close binaries, either in binaries or triples are indeed important for BSS formation pathway in OCs.

5 SUMMARY

The work presented in this paper can be summarized as follows:

(i) We identified 2175 cluster members in NGC 2506 using a machine learning based algorithm, ML–MOC, on *Gaia* EDR3 data including nine BSS, three YSS, and three RC stars. We present the analysis of these BSS, YSS, and RC stars using *ASTROSAT*/UVIT data in three FUV filters, *F148W*, *F154W*, and *F169M*.

(ii) The multiwavelength SEDs of only seven BSS were constructed as two of them had neighbours within 3 arcsec. Out of seven BSS, we found that four BSS fitted well with a single-temperature SED, whereas three showed an excess greater than 30 per cent from the best-fitting model. These three BSS were fitted with double-component SEDs and the properties of the hot companions are reported in this work.

(iii) The temperatures of BSS of NGC 2506 varies from 7750 to 9750 K, which are consistent with the young age of the cluster. The temperatures of YSS varies from 6500 to 6750 K, whereas the temperatures of RC stars varies from 5000 to 5250 K.

(iv) We discover two ELM WD and one LM WD as companions to three BSS in the cluster. One of the ELM WD of mass ~ 0.18 M$_\odot$ is found as a companion to BSS1. Its temperature is estimated to be 13 250 K, luminosity to be 0.44 L$_\odot$, and radius to be 0.13 R$_\odot$. The second ELM also of mass ~ 0.18 M$_\odot$ is found as a companion of BSS2. It has temperature $\sim 15\,000$ K, luminosity ~ 0.45 L$_\odot$, and radius ~ 0.10 R$_\odot$. The LM WD of mass ~ 0.20 M$_\odot$ is found as a companion to BSS8 with $T_{\rm eff} \sim 19\,000$ K, $L \sim 0.24$ L$_\odot$, and $R \sim 0.05$ R$_\odot$. The hot companions of these BSS have log age ~ 7.5–8.5.

(v) We also constructed the SEDs of the three YSS and three RC candidates that were detected in UVIT/FUV filters. All these six objects showed an excess in FUV data points indicating the presence of a hotter companion. We fitted the double-component SEDs of all RCs and YSS (except YSS2). From the parameters ($T_{\rm eff} \sim 29\,000$–$31\,000$ K, $L \sim 0.05$–0.14 L$_\odot$, and $R \sim 0.01$ R$_\odot$) of the hot companions of YSS1, RC1, and RC2, we infer that they are likely to be normal mass (~ 0.6 M$_\odot$) WDs, suggesting to be formed from the star of mass 1.45 M$_\odot$, which is the cluster turn-off mass. However, the presence of high-mass (~ 0.8 M$_\odot$) WD with parameters $T_{\rm eff} \sim 26\,000$–$31\,000$ K, $L \sim 0.07$–0.09 L$_\odot$, and $R \sim 0.01$ as the companions of YSS3 and RC3 indicates the presence of their massive progenitors such as BSS. Thus, these two systems may likely have formed from triplets.

(vi) We conclude that in the OC NGC 2506, the Case A/Case B mass transfer mechanism is likely to be responsible for the formation of at least 4 out of 10 (40 per cent) BSS and YSS systems. However, the merger in triple system with close inner binary is the potential formation pathway of YSS and RC stars with BSS as their progenitors.

DATA AVAILABILITY

The data underlying this paper are publicly available at https://astrobrowse.issdc.gov.in/astro_archive/archive/Home.jsp The derived data generated in this research will be shared on reasonable request to the corresponding author.

REFERENCES

Agarwal M., Rao K. K. K., Bhattacharya S., 2021, MNRAS, 502, 2582

Ahumada J., Lapasset E., 1995, A&AS, 109, 375

Althaus L. G., Bertolami M. M. M., Córsico A. H., 2013, A&A, 557, A19

Anthony-Twarog B. J., Deliyannis C. P., Twarog B. A., 2016, AJ, 152, 192

Anthony-Twarog B. J., Lee-Brown D. B., Deliyannis C. P., Twarog B. A., 2018, AJ, 155, 138

Arentoft T. et al., 2007, A&A, 465, 965

Babusiaux C. et al., 2022, A&A, preprint (arXiv:2206.05989)

Bailyn C. D., 1995, ARA&A, 33, 133

Bayo A., Rodrigo C., Navascus Y, 2008, A&A, 492, 277

Beccari G., Ferraro F. R., Lanzoni B., Bellazzini M., 2006, ApJ, 652, L121

Bianchi L. et al., 2000, Mem. Soc. Astron. Ital., 71, 1123

Bressan A., Marigo P., Girardi L., Salasnich B., Dal Cero C., Rubele S., Nanni A., 2012, MNRAS, 427, 127

Brown W. R., Kilic M., Prieto C. A., Kenyon S. J., 2010, ApJ, 723, 1072

Brown J. M., Kilic M., Brown W. R., Kenyon S. J., 2011, ApJ, 730, 67

Carretta E., Bragaglia A., Gratton R., Tosi M., 2004, A&A, 422, 951

Castelli F., Gratton R., Kurucz R., 1997, A&A, 318, 841

Chambers K. C. et al., 2016, preprint (arXiv:1612.05560)

Chatterjee S., Rasio F. A., Sills A., Glebbeek E., 2013, ApJ, 777, 106

Chen X., Han Z., 2008, MNRAS, 384, 1263

Clark L. L., Sandquist E. L., Bolte M., 2004, AJ, 128, 3019

Coelho P. R. T., 2014, MNRAS, 440, 1027

Cohen M., Wheaton W. A., Megeath S., 2003, AJ, 126, 1090

Cover T., Hart P., 1967, IEEE Trans. Inf. Theory, 13, 21

De Angeli F. et al., 2022, A&A, preprint (arXiv:2206.06143)

Eyer L. et al., 2022, A&A, preprint (arXiv:2206.06416)

Fabrycky D., Tremaine S., 2007, ApJ, 669, 1298

Ferraro F., Fusi Pecci F., Buonanno R., 1992, MNRAS, 256, 376

Ferraro F. et al., 2006, ApJ, 647, L53

Ferraro F. et al., 2012, Nature, 492, 393

Ferraro F. et al., 2018, ApJ, 860, 36

Fiorentino G., Lanzoni B., Dalessandro E., Ferraro F., Bono G., Marconi M., 2014, ApJ, 783, 34

Fitzpatrick E. L., 1999, PASP, 111, 63

Friel E., Janes K., 1993, A&A, 267, 75

Gaia Collaboration et al., 2021, A&A, 649, A1

Gilliland R. L., Bono G., Edmonds P. D., Caputo F., Cassisi S., Petro L. D., Saha A., Shara M. M., 1998, ApJ, 507, 818

Girardi L., 2016, ARA&A, 54, 95

Gosnell N. M., Mathieu R. D., Geller A. M., Sills A., Leigh N., Knigge C., 2015, ApJ, 814, 163

Hidalgo S. L. et al., 2018, ApJ, 856, 125

Hunter J., Dale D., 2007, Matplotlib 0.90. 0 user's guide

Hurley J. R., Pols O. R., Aarseth S. J., Tout C. A., 2005, MNRAS, 363, 293

Hypki A., Giersz M., 2013, MNRAS, 429, 1221

Indebetouw R. et al., 2005, ApJ, 619, 931

Jadhav V. V., Subramaniam A., 2021, MNRAS, 507, 1699

Jadhav V. V., Pandey S., Subramaniam A., Sagar R., 2021a, J. Astrophys. Astron., 42, 89

Jadhav V. V., Pennock C. M., Subramaniam A., Sagar R., Nayak P. K., 2021b, MNRAS, 503, 236

Jiménez-Esteban F., Torres S., Rebassa-Mansergas A., Skorobogatov G., Solano E., Cantero C., Rodrigo C., 2018, MNRAS, 480, 4505

Kharchenko N., Piskunov A., Schilbach E., Röser S., Scholz R.-D., 2013, A&A, 558, A53

Kim S.-L. et al., 2001, Acta Astron., 51, 49

Kiseleva L., Eggleton P., Mikkola S., 1998, MNRAS, 300, 292

Knigge C., Shara M. M., Zurek D. R., Long K. S., Gilliland R. L., 2000, preprint (arXiv:astro-ph/0012187)

Knigge C., Leigh N., Sills A., 2009, Nature, 457, 288

Knudstrup E. et al., 2020, MNRAS, 499, 1312

Koester D., 2010, Mem. Soc. Astron. Ital., 81, 921

Kumar A. et al., 2012, in Takahashi T., Murray S. S., den Herder J.-W. A., eds, Proc. SPIE Conf. Ser. Vol. 8443, Space Telescopes and Instrumentation 2012: Ultraviolet to Gamma Ray. SPIE, Bellingham, p. 84431N

Landsman W., Aparicio J., Bergeron P., Di Stefano R., Stecher T., 1997, ApJ, 481, L93

Leigh N., Sills A., Knigge C., 2011, MNRAS, 416, 1410

Leiner E., Mathieu R. D., Stello D., Vanderburg A., Sandquist E., 2016, ApJ, 832, L13

McClure R., Twarog B., Forrester W., 1981, ApJ, 243, 841

McCrea W., 1964, MNRAS, 128, 147

Martin D. C. et al., 2005, ApJ, 619, L1

Mathieu R. D., Geller A. M., 2009, Nature, 462, 1032

Millman K. J., Aivazis M., 2011, Comput Sci Eng., 13, 9

Momany Y., Held E., Saviane I., Zaggia S., Rizzi L., Gullieuszik M., 2007, A&A, 468, 973

Oliphant T. E. et al., 2007, Comput Sci Eng., 9, 10

Pandey S., Subramaniam A., Jadhav V. V., 2021, MNRAS, 507, 2373

Panei J. A., Althaus L. G., Chen X., Han Z., 2007, MNRAS, 382, 779

Peel D., McLachlan G. J., 2000, Stat. Comput., 10, 339

Perets H. B., Fabrycky D. C., 2009, ApJ, 697, 1048

Pérez F., Granger B. E., 2007, Comput Sci Eng., 9, 21

Postma J. E., Leahy D., 2017, PASP, 129, 115002

Postma J. E., Leahy D., 2021, J. Astrophys. Astron., 42, 1

Preston G. W., Sneden C., 2000, AJ, 120, 1014

Price-Whelan A. M. et al., 2018, AJ, 156, 123

Rain M., Ahumada J., Carraro G., 2021, A&A, 650, A67

Rangwal G., Yadav R., Durgapal A., Bisht D., Nardiello D., 2019, MNRAS, 490, 1383

Rao K. K., Vaidya K., Agarwal M., Bhattacharya S., 2021, MNRAS, 508, 4919

Rebassa-Mansergas A. et al., 2021, MNRAS, 506, 5201

Reddy A. B., Giridhar S., Lambert D. L., 2012, MNRAS, 419, 1350

Sahu S., Subramaniam A., Côté P., Rao N. K., Stetson P. B., 2018, MNRAS, 482, 1080

Sandage A., 1953, AJ, 58, 61

Shara M. M., Saffer R. A., Livio M., 1997, ApJ, 489, L59

Siegel M. H. et al., 2014, AJ, 148, 131

Sindhu N. et al., 2019, ApJ, 882, 43

Stetson P. B., 1987, PASP, 99, 191

Stryker L., 1993, PASP, 105, 1081

Subramaniam A. et al., 2016a, ApJ, 833, L27

Subramaniam A. et al., 2016b, in den Herder J.-W. A., Takahashi T., Bautz M., eds, Proc. SPIE Conf. Ser. Vol. 9905, Space Telescopes and Instrumentation 2016: Ultraviolet to Gamma Ray. SPIE, Bellingham, p. 99051F

Tandon S. et al., 2017, AJ, 154, 128

Tandon S. et al., 2020, AJ, 159, 158

Taylor M., 2011, Astrophysics Source Code Library, record ascl:1105.003

Tremblay P.-E., Bergeron P., 2009, ApJ, 696, 1755

Vaidya K., Rao K. K., Agarwal M., Bhattacharya S., 2020, MNRAS, 496, 2402

Vaidya K., Panthi A., Agarwal M., Pandey S., Rao K. K., Jadhav V., Subramaniam A., 2022, MNRAS, 511, 2274

Webbink R., 1976, ApJ, 209, 829

Wright E. L. et al., 2010, AJ, 140, 1868

Xin Y., Deng L., 2005, ApJ, 619, 824

This paper has been typeset from a TEX/LATEX file prepared by the author.